Satellite Long-Term Monitoring of Wetland Ecosystem Functioning in Ramsar Sites for Their Sustainable Management

Quentin Demarquet, Sébastien Rapinel, Damien Arvor, Samuel Corgne, Laurence Hubert-Moy

▶ **To cite this version:**

Quentin Demarquet, Sébastien Rapinel, Damien Arvor, Samuel Corgne, Laurence Hubert-Moy. Satellite Long-Term Monitoring of Wetland Ecosystem Functioning in Ramsar Sites for Their Sustainable Management. Sustainability, 2024, 16 (15), pp.6301. 10.3390/su16156301 . hal-04692001

HAL Id: hal-04692001
https://hal.science/hal-04692001v1

Submitted on 9 Sep 2024

HAL is a multi-disciplinary open access archive for the deposit and dissemination of scientific research documents, whether they are published or not. The documents may come from teaching and research institutions in France or abroad, or from public or private research centers.

L'archive ouverte pluridisciplinaire **HAL**, est destinée au dépôt et à la diffusion de documents scientifiques de niveau recherche, publiés ou non, émanant des établissements d'enseignement et de recherche français ou étrangers, des laboratoires publics ou privés.

sustainability

MDPI

Article

Satellite Long-Term Monitoring of Wetland Ecosystem Functioning in Ramsar Sites for Their Sustainable Management

Quentin Demarquet, Sébastien Rapinel *, Damien Arvor, Samuel Corgne and Laurence Hubert-Moy

LETG UMR 6554, Geography Department, Université Rennes 2, Centre National de la Recherche Scientifique (CNRS), Place du Recteur Henri Le Moal, 35000 Rennes, France; quentin.demarquet@univ-rennes2.fr (Q.D.); damien.arvor@univ-rennes2.fr (D.A.); samuel.corgne@univ-rennes2.fr (S.C.); laurence.moy@univ-rennes2.fr (L.H.-M.)
* Correspondence: sebastien.rapinel@univ-rennes2.fr

Abstract: The long-term monitoring of wetland ecosystem functioning is critical because wetlands, which provide multiple services, can be affected by human activities and climate change. The aim of this study was to monitor wetland ecosystem functioning in the long term using the Landsat archive. Four contrasting, Ramsar wetlands were selected in boreal, temperate, arid, and tropical areas. First, the annual sum of the normalized difference vegetation index (NDVI-I) was calculated as an indicator of annual net primary productivity for the period 1984–2021 using the continuous change detection and classification (CCDC) algorithm. Next, the influence of the number of Landsat images and class of land use and land cover (LULC) on the accuracy of the CCDC was investigated. Finally, correlations between annual NDVI-I and climate were analyzed. The results revealed that NDVI-I accuracy was influenced mainly by the LULC class and to a lesser extent by the number of cloud-free Landsat observations. Infra- and inter-site variations in NDVI-I were high and showed an overall increasing trend. NDVI-I was positively correlated with the mean temperature. This study shows that this approach applied in contrasting sites is robust for the long-term monitoring of wetland ecosystem functioning and can be used to improve the implementation of international biodiversity conservation policies.

Keywords: Landsat; Google Earth Engine; CCDC; ecosystem degradation; biodiversity preservation

check for updates

Citation: Demarquet, Q.; Rapinel, S.; Arvor, D.; Corgne, S.; Hubert-Moy, L. Satellite Long-Term Monitoring of Wetland Ecosystem Functioning in Ramsar Sites for Their Sustainable Management. *Sustainability* **2024**, *16*, 6301. https://doi.org/10.3390/su16156301

Academic Editor: Changwoo Ahn

Received: 29 June 2024
Revised: 17 July 2024
Accepted: 19 July 2024
Published: 23 July 2024

Copyright: © 2024 by the authors. Licensee MDPI, Basel, Switzerland. This article is an open access article distributed under the terms and conditions of the Creative Commons Attribution (CC BY) license (https://creativecommons.org/licenses/by/4.0/).

1. Introduction

Although wetlands support many functions and ecosystem services [1], they have been increasingly threatened over the past several decades due to climate change and human pressure [2]. In this context, international biodiversity conservation policies have been implemented, such as the Ramsar Convention [3], the Aichi Targets of the Convention on Biological Diversity [4], the UN Sustainable Development Goals [5], and the Paris Climate Agreement [6]. However, these policies are difficult to implement due to the incomplete evaluation of the ecological character of wetlands, which considers the composition and structure of these ecosystems but not their functioning [7,8]. However, the scientific community has shown that indicators of the long-term functioning of wetlands can be derived from satellite time series [8,9]. A number of wetland conservation initiatives based on Earth Observation (EO) data have been implemented worldwide, such as the Globwetland Program [10], the Satellite-Based Wetland Observation Service Project [11], and the Ramsar Reporting Convention [12]. The studies conducted as part of these initiatives highlighted the need for the systematic assessment of the accuracy, relevance, and transferability of EO-derived products, as well as for the long-term continuous monitoring of wetlands at high spatial resolution using an EO archive [13].

While different open access satellite data sources could be used for long-term wetland monitoring, Landsat imagery was selected because it combines a long observation period (40 years) with a high spatial resolution (30 m) [14] compared to Sentinel-2 imagery (9 years,

10 m) or MODIS imagery (23 years, 250 m). The Landsat program provides unique capabilities for observing the entire Earth for 40 years at 30 m spatial resolution [14]. Landsat images were acquired every 16 days by Landsat 4–7 (1984–2022) and have been acquired every 8 days by Landsat 8–9 (2013–present). The Landsat archive, which the U.S. Geological Survey has provided free of charge since 2008 [15], can be easily accessed and processed using cloud-computing platforms such as the Google Earth Engine (GEE) [16]. Although the Landsat archive is increasingly used for the long-term monitoring of wetlands, it has not been fully exploited, as cloudy images and images influenced by the failure of the SLC on Landsat 7 have been discarded. This has resulted in discontinuous time series that may exclude periods when ecosystems changed greatly [17].

The entire Landsat archive can now be turned into a continuous time series to generate a synthetic image for any date using harmonic regression methods [18]. Among these methods, the CCDC algorithm is the most widely used for ecosystem monitoring using Landsat data [19], as it is suited to time series with many missing observations at the pixel scale [20] and is easily accessible using cloud-computing tools [21]. While the CCDC algorithm has been widely used for classification, it has been under-used for producing synthetic images [19] to derive indicators of ecosystem functioning [22]. For example, continuous long-term time series derived from the Landsat archive using the CCDC algorithm have better captured subtle changes and seasonal variations in biomass in tropical [23] and semi-arid [24] forests, or phenology in a temperate marsh [25]. However, the worldwide relevance and transferability of the CCDC in producing continuous long-term indicators of ecosystem functioning such as annual net primary productivity (ANPP) has not been evaluated.

In this study, wetland ecosystem functioning refers to their annual greenness cycle of vegetation, and the NDVI-I index was used as a surrogate of ANPP. This index is a reliable indicator of wetland ecosystem functioning, such as carbon storage and fluxes [26] or habitat support [27]. ANPP has high spatial and temporal variability in wetlands and responds to human and climate disturbances [28,29]. ANPP can be derived from continuous satellite-based time series of the NDVI, as the latter, which is strongly correlated with aboveground net primary productivity, is a linear estimator of the fraction of photosynthetically active radiation absorbed by vegetation, the main driver of primary production [30]. Thus, the annual NDVI integral (NDVI-I), which equals the sum of NDVI and represents ANPP, can be used as an integrated indicator of wetland ecosystem functioning [22]. To date, monitoring ANPP using EO data in wetlands has meant a trade-off between the duration of monitoring and spatial resolution: either long-term at low spatial resolution [31] or short-term at high spatial resolution [28]. However, the long-term monitoring of ANPP at high spatial resolution is now possible using the Landsat archive [32].

The aim of this study was to monitor long-term changes in wetland ecosystem functioning using the Landsat archive and the CCDC algorithm. Specifically, we explored the influence of the LULC class and the number of available cloud-free Landsat observations for each pixel on the accuracy of the NDVI-I, as harmonic regression methods are likely to perform better when applied to stable ecosystems with many cloud-free observations. Four Ramsar wetlands were selected in boreal, temperate, arid, and tropical biomes to cover a wide range of LULC classes and cloud-free Landsat observation numbers.

2. Materials and Methods

2.1. Study Sites

This study focused on four Ramsar wetlands that covered a wide range of wetland types and cloud-free Landsat observation numbers due to bioclimatic conditions (Figure 1). The first site is a 2586 ha unexploited tundra mire complex in northern Sweden (*Pirttimysvuoma*, Ramsar ID 2177) frequently grazed by reindeer. Due to the site's high latitude and boreal climate, it had the fewest cloud-free Landsat observations (Figure 1A).

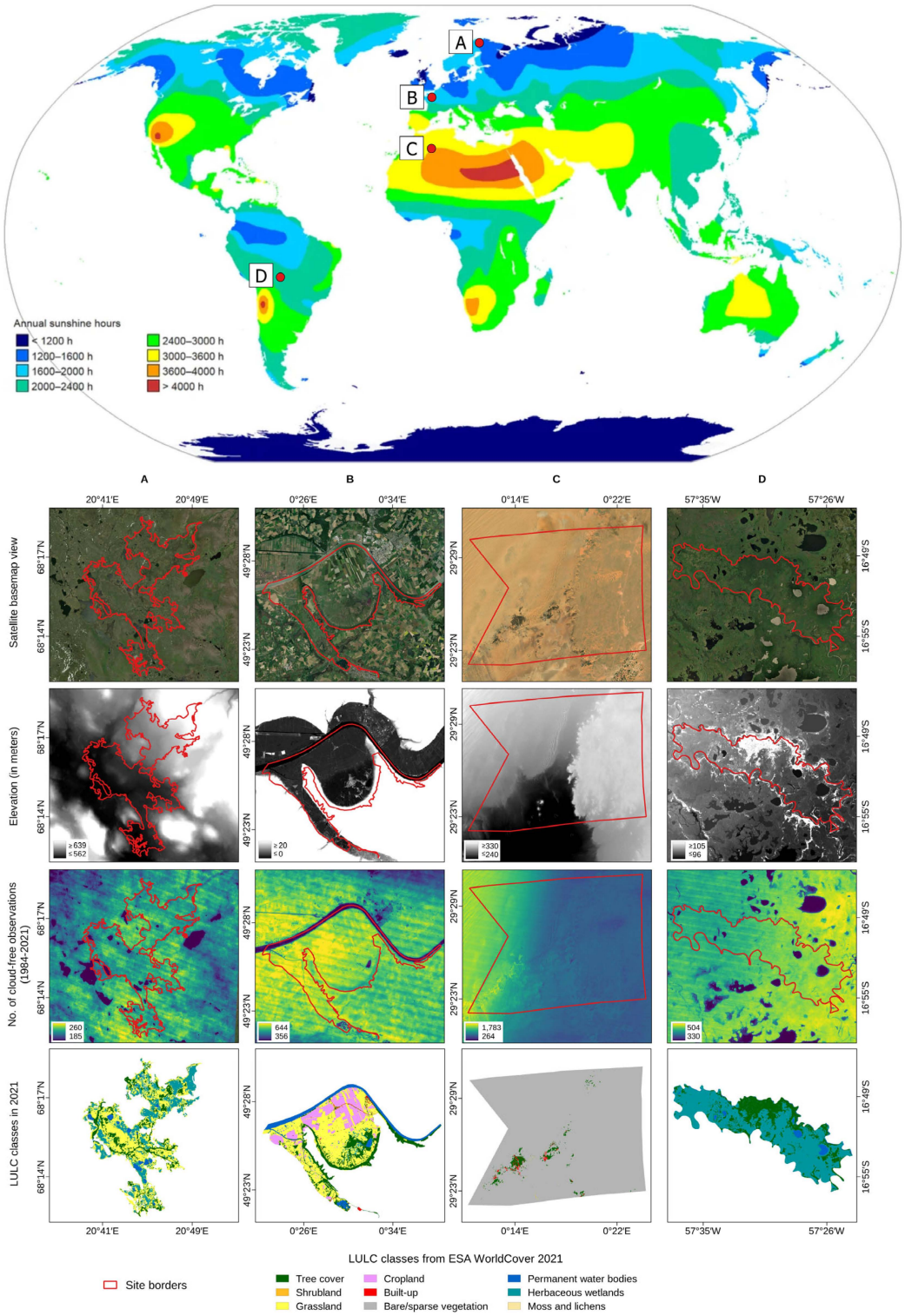

Figure 1. Top: Location of the four Ramsar wetland sites on a world map of the annual hours of sunshine [33]: (**A**) Pirttimysvuoma; (**B**) Marais Vernier; (**C**) Ouled Saïd; (**D**) Taiamã Ecological Station. Bottom: View of the four Ramsar wetland sites as Google Earth images (first row), the elevation derived from the Copernicus DEM (second row), the number of cloud-free Landsat observations (third row), and the LULC classes in 2021 (fourth row).

The second site, the Marais Vernier et Vallée de la Risle Maritime (Ramsar ID 2247), is located in France and has a temperate climate. This 9565 ha site is dominated by seasonally

flooded agricultural land. A moderate number of cloud-free Landsat observations were available for this site (Figure 1B).

The third site, Oasis de Ouled Saïd (Ramsar ID 1060), is located in the Sahara Desert. This 25,400 ha oasis wetland developed in a former channel bed. Due to this site's arid climate, many cloud-free Landsat observations were available for it (Figure 1C).

The fourth site, the Taiamã Ecological Station (Ramsar ID 2363) covers 11,555 ha in the Pantanal wetland (Figure 1D). This tropical wetland is dominated by seasonal and permanent freshwater marshes and is frequently threatened by fires. Few cloud-free Landsat observations were available due to the frequency of tropical rainfall.

A more detailed description of each site is provided on the Ramsar Sites Information Service website (https://rsis.ramsar.org/ (accessed on 17 July 2024)).

2.2. Data

2.2.1. Landsat Archive

Level-2 Landsat atmospherically corrected surface reflectance images were extracted for 1984–2021 from the Landsat Collection 2 archive [34], which is available in the GEE [35]. Specifically, the images were acquired using the Landsat 4–5 thematic mapper (TM), Landsat 7 enhanced thematic mapper (ETM+), and Landsat 8–9 operational land imager (OLI) sensors (Figure 2). The Landsat 1–2–3 Multispectral Scanner archive was not used in this study because the spectral and spatial characteristics of this sensor differ greatly from those of the other Landsat sensors. All available images were considered, including cloudy images and Landsat 7 SLC-off images, as the CCDC algorithm contains a two-step cloud, cloud shadow, and snow-masking tool to eliminate "noisy" observations [36]. In total, 1263, 2090, 2715, and 929 Landsat images were used for the Pirttimysvuoma, Marais Vernier, Ouled Saïd, and Taiamã, respectively (Figure 2, Appendix A (Table A1)).

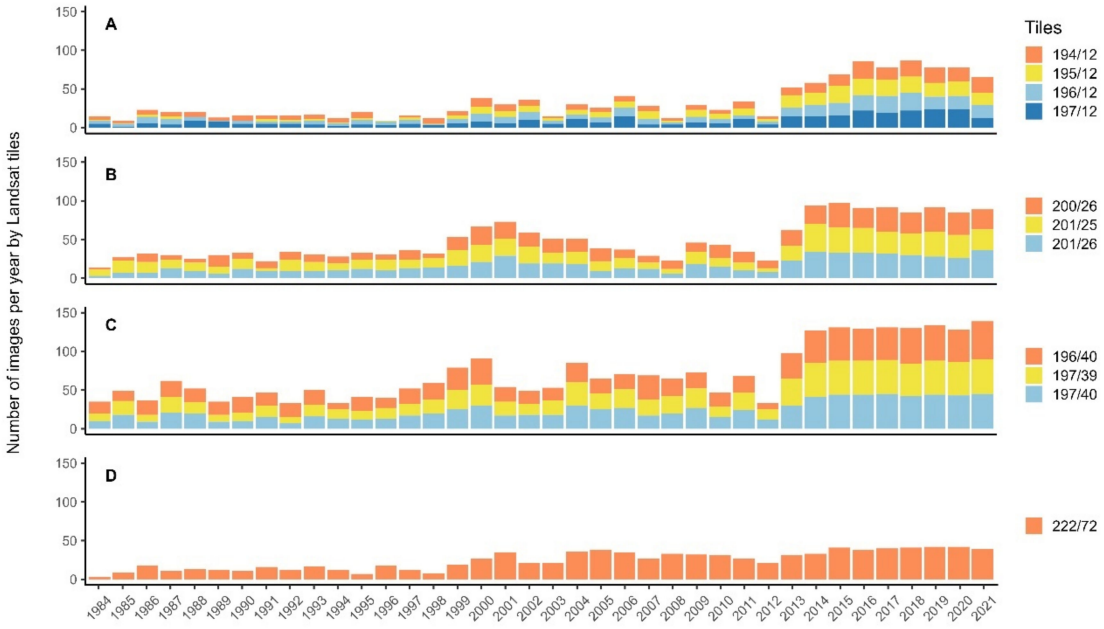

Figure 2. Number of Landsat images by tile per year for each site: (**A**) Pirttimysvuoma; (**B**) Marais Vernier; (**C**) Ouled Saïd; (**D**) Taiamã Ecological Station.

Landsat images were pre-processed in the CCDC GEE application program interface (API) [21] using a two-step procedure: noisy pixels were masked using the quality-assessment band, and clouds, cloud shadows, and snow cover were removed using CFmask [37], a C programming language translation of the Fmask version 3.2 algorithm [38] (Figure 3).

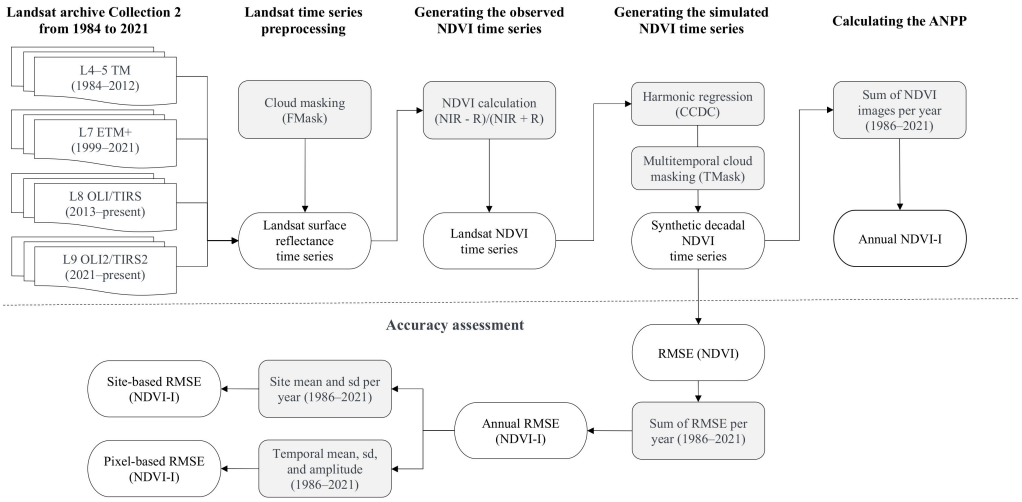

Figure 3. The method used to calculate the annual normalized difference vegetation index integral (NDVI-I) as an indicator of annual net primary productivity (ANPP) using the continuous change detection and classification (CCDC) application program interface [21]. RMSE: root-mean-square error, SD: standard deviation.

2.2.2. LULC Data

The ESA WorldCover 2021 version 200 raster map was downloaded from the Zenodo repository [39]. The map, which contains 11 LULC classes aligned with the UN-FAO Land Cover Classification System, was produced from the Sentinel-1&2 time series. It has a spatial resolution of 10 m and an overall accuracy of 77%.

2.2.3. Climatic Data

Gridded climate data were retrieved for 1984–2021 at 0.5° spatial resolution from the Global Historical Climatology Network - Daily (GHCN-d) dataset [40] of the NOAA Climate Prediction Center (CPC) [41], which contains records from more than 100,000 stations in 180 countries and territories. These climate data were gridded using the Shepard algorithm. The distance of Pirrtimysvuoma, Marais Vernier, Ouled Saïd, and Taiamã Ecological Station to the nearest GHCN meteorological station was 61, 26, 23, and 29 km, respectively. Daily minimum (T_{min}) and maximum (T_{max}) temperatures were extracted for each site from the CPC Global Unified Temperature product and then averaged per year. Daily mean temperature (T_{mean}) was calculated as the mean of daily T_{min} and daily T_{max} and then averaged per year. Daily precipitation (P_{mm}) was extracted for each site from the CPC Global Unified Gauge-Based Analysis of Daily Precipitation product and then summed per year.

2.3. Calculating Indicator of Wetland Ecosystem Functioning

As a reliable indicator of ecosystem primary productivity [30], a continuous time series of the NDVI was calculated in the cloud using the CCDC API [21] to estimate the ANPP (Figure 3).

2.3.1. Generating the Observed NDVI Time Series

A discontinuous time series was generated for each 30 m pixel by calculating the NDVI from each cloud-masked Landsat image using the following equation:

$$NDVI = (NIR - Red)/(NIR + Red) \quad (1)$$

where NIR corresponds to the near-infrared spectrum (band 4: 0.76–0.90 µm for the TM and ETM+ sensors and band 5: 0.85–0.88 µm for the OLI sensor) and Red to the red spectrum (band 3: 0.63–0.69 µm for the TM and ETM+ sensors and band 4: 0.64–0.67 µm for the OLI sensor).

2.3.2. Generating the Simulated NDVI Time Series

A continuous simulated NDVI time series was generated for each 30 m pixel using a harmonic regression model that was fit to a stable historical period at the beginning of the observed NDVI time series. Next, new observations (pixels) were added to the model iteratively, and their residuals were compared to the root-mean-square error (RMSE) of the historical period. When the predictions differed significantly from the observations on six consecutive dates (i.e., when residuals of future observations exceeded a chi-square threshold value), a break (indicating a potential change in the structure or functioning of the wetland) was flagged, and a new model was initialized. This process was repeated for the remaining observations of the NDVI time series (Figure 4). The multi-temporal Tmask algorithm [42] was also applied during this procedure to remove aberrant observations not detected by the Fmask algorithm before fitting the harmonic model.

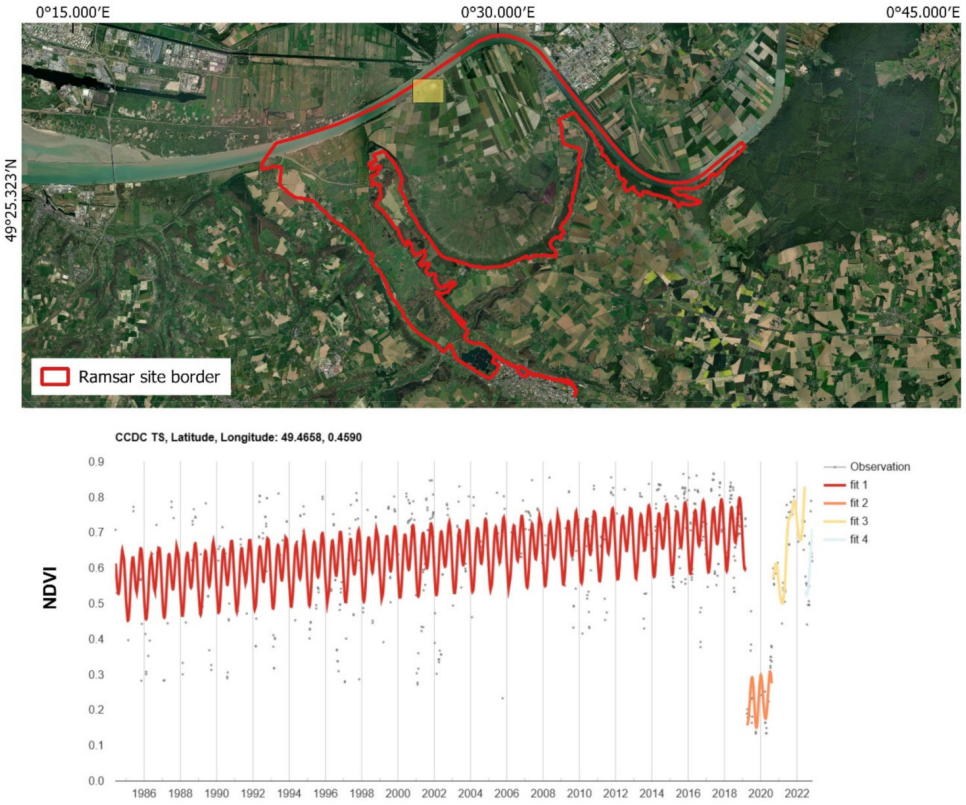

Figure 4. Example of the normalized difference vegetation index (NDVI) time series (TS) extracted from the Landsat archive for 1984–2021 at the Marais Vernier Ramsar site. The yellow rectangle identifies the pixel from which the time series was extracted and analyzed using the continuous change detection and classification (CCDC) algorithm. The colored lines indicate fits during time segments detected by the CCDC algorithm; a change in color indicates a change in land cover/land use.

The CCDC API provides two types of harmonic models: ordinary least-square regression and least absolute shrinkage and selection operator (LASSO) regression. The latter was selected because it has a regularization parameter that reduces overfitting [43] and remains robust when only a few cloud-free Landsat images are available during a year [44]. CCDC also provides the RMSE for each band, which indicates the accuracy with which the observed reflectance was predicted.

To evaluate the transferability of the CCDC algorithm, it was applied with the default parameters set in the API (Table 1) to each Landsat pixel for specific dates each year for each study site. It should be noted that the default parameters in the help document (https://developers.google.com/earth-engine/apidocs/ee-algorithms-temporalsegmentation-ccdc

(accessed on 17 July 2024)) and given in the literature [19,23] differed slightly from those in the submit_CCDC script used (https://code.earthengine.google.com/?accept_repo=users/parevalo_bu/gee-ccdc-tools (accessed on 17 July 2024)). In total, 1388 synthetic mean NDVI images at a 10-day time step were generated for each site from 1984 to 2021. This decadal interval was considered a reasonable trade-off between temporal resolution and computing requirements. The model RMSE per period and the number of breaks in the time series were retrieved from CCDC outputs for each Landsat pixel of the four sites.

Table 1. Parameters for the continuous change detection and classification algorithm and default values set in the API submit_ccdc script (https://code.earthengine.google.com/?accept_repo=users/parevalo_bu/gee-ccdc-tools (accessed on 17 July 2024)) applied to the four study sites. Asterisks indicate non-default values.

Parameter	Meaning	Value
breakpointBands	The name or index of the bands used for change detection	NDVI *
tmaskBands	The name or index of the bands used for iterative TMask cloud detection	Green, SWIR2
MinObs	Moving window size for break detection	5
Lambda	Penalty parameter for LASSO regression	0.005
ChiSquareProbability	Chi-square probability threshold for break detection	0.99 *
MinNumOfYearsScaler	Minimum number of years before applying a new fitting	1.33
Seg	Maximum number of temporal segments in the entire time series	6
MaxIterations	Maximum number of runs for LASSO regression convergence	10,000 *

2.3.3. Calculating NDVI-I

The NDVI-I is a reliable indicator of the ANPP [45]. Before calculating the NDVI-I, the years 1984–1985 were removed as they corresponded to the initialization of the first harmonic model, which had predicted many "no data" values on the synthetic NDVI images. The NDVI-I was then calculated for each year and each site by setting negative NDVI values to zero (to avoid water-related biases) and summing the decadal synthetic NDVI images. As a result, the NDVI-I theoretically ranged from 0.0 (0 × 36 images) to 36.0 (1 × 36 images), and as NDVI-I values increased, ANPP increased.

To investigate spatiotemporal variations in the accuracy of NDVI-I, annual cumulative RMSE images—corresponding to the sum of the RMSE of model predictions of decadal synthetic NDVI images for the year—were generated per pixel for each site. Spatiotemporal variations in the NDVI-I for 1986–2021 were assessed for each site by calculating, for each pixel, the temporal mean, temporal standard deviation (SD), and temporal amplitude of NDVI-I, as well as the two years with the minimum and maximum NDVI-I.

2.4. Influence of LULC Class and Number of Cloud-Free Landsat Observations on NDVI-I Accuracy

To investigate the influence of LULC on NDVI-I accuracy, we used the 2021 ESA WorldCover map [39] instead of the CCDC classification output to ensure independence between LULC and NDVI-I values. The cumulative RMSE of the synthetic NDVI images for 2021, the LULC classes, and the number of Landsat cloud-free observations available in 2021 (divided into five classes using the Jenks natural breaks method: very small (0–6), small (7–19), moderate (20–35), large (36–63), and very large (64–113)) were extracted for each Landsat pixel at each site. Under-represented (<100 pixels per site) combinations of LULC class and observation number (e.g., grasslands and very large) were removed from the analysis. Eighty pixels were then randomly selected from each combination of LULC class and observation number. For each site, permutational Type II analysis of variance (ANOVA) (i.e., with no assumptions about normality or heteroscedasticity [46]) was performed with the selected pixels to estimate the RMSE as a function of LULC class and the number of observations. The size of RMSE variance explained by each factor and their interaction was expressed by the partial eta-squared index (η^2) [47] as follows:

$$\eta^2 = SS_{effect} / (SS_{effect} + SS_{error}) \quad (2)$$

where SS_{effect} is the sum of squares associated with the effect of the factor, and SS_{error} is the sum of squares error (i.e., unexplained variance) in the ANOVA model.

To reduce the bias due to sample balancing, pixels were randomly selected, and the ANOVA was repeated 500 times.

2.5. Correlation between NDVI-I and Climate Data

For each site, the correlation between annual climate variables (i.e., mean T_{min}, mean T_{max}, mean T_{mean}, and cumulative P_{mm}) and spatially averaged annual NDVI-I for 1986–2021 was assessed using the Pearson correlation coefficient. Statistical analyses were performed using R software version 3.3 [48] with the terra [49], FactoMineR [50], and lmPerm [51] packages.

3. Results

3.1. CCDC Sensitivity

The sensitivity of the CCDC algorithm for the wetland sites varied at the site scale (Figure 5) and pixel scale (Figure 6). At the site scale, the CCDC algorithm was consistently accurate when generating NDVI-I for 1986–2021. The slope of the trend in RMSE ranged from −0.010 for Taiamã (Figure 5D) to 0.002 for Marais Vernier (Figure 5B). NDVI-I accuracy was higher and less variable for Ouled Saïd (mean RMSE: 0.44–0.49, SD of RMSE: 0.17–0.19) (Figure 5C) and Pirrtimysvuoma (mean RMSE: 2.63–2.70, SD of RMSE: 0.49–0.51) (Figure 5A) than for Marais Vernier (mean RMSE: 3.80–4.03, SD of RMSE: 1.38–1.54) (Figure 5B) and Taiamã (mean RMSE: 1.89–2.38, SD of RMSE: 0.94–1.51). For Taiamã, the RMSE decreased continuously beginning in the 2000s (Figure 5D).

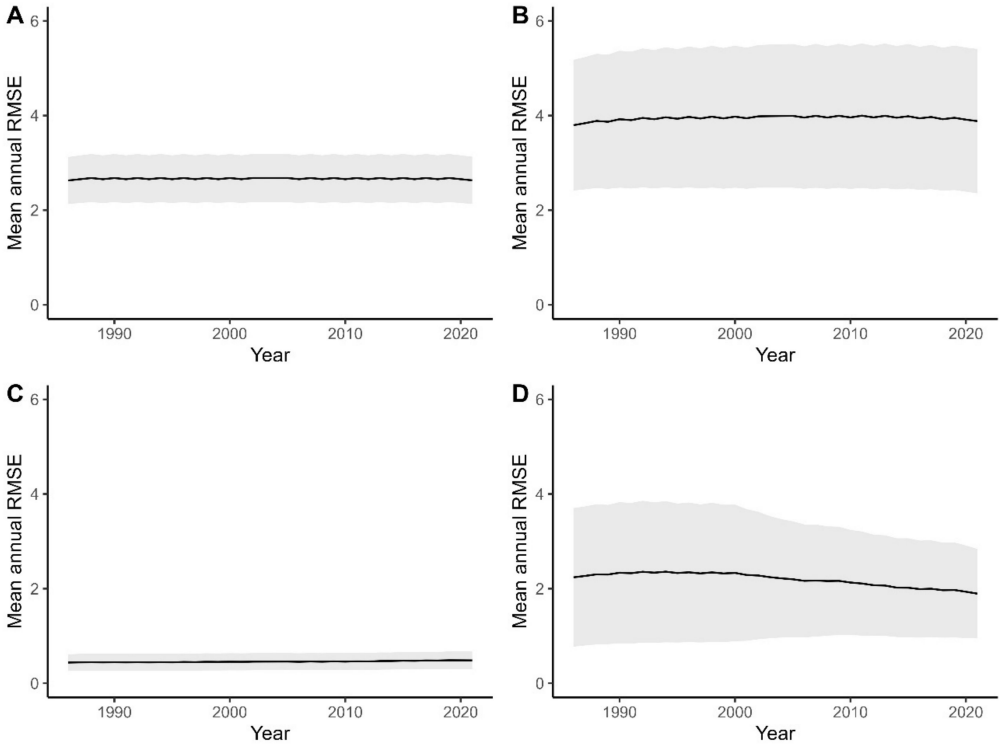

Figure 5. Annual variation in spatially averaged root-mean-square error (RMSE) of the annual normalized difference vegetation index integral (NDVI-I) (black line) and standard deviation (grey area) calculated from all pixels for each site from 1986 to 2021: (**A**) Pirttimysvuoma; (**B**) Marais Vernier; (**C**) Ouled Saïd; (**D**) Taiamã Ecological Station.

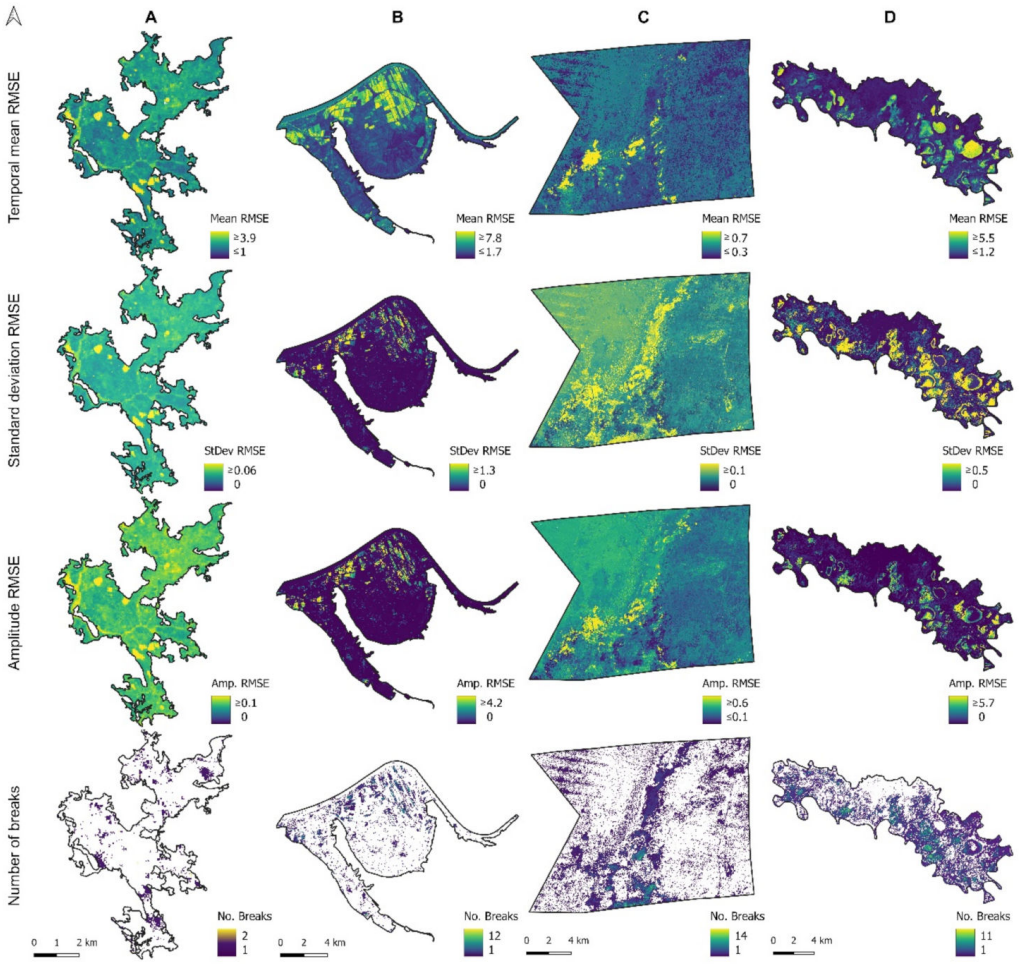

Figure 6. Temporal mean, standard deviation (StDev), and amplitude (Amp.) of the annual normalized difference vegetation index integral (NDVI-I) root-mean-square error (RMSE) and number of breaks (No. Breaks) detected in the NDVI time series using the continuous change detection and classification algorithm for the four study sites from 1986 to 2021. Image stretching was applied to each site to highlight its spatial pattern. (**A**) Pirttimysvuoma; (**B**) Marais Vernier; (**C**) Ouled Saïd; (**D**) Taiamã Ecological Station.

At the pixel scale, NDVI-I accuracy had a fine-grained pattern for all sites (Figure 6). For Pirttimysvuoma, scattered patches of larger RMSE (mean $\geq$ 3.90, SD $\geq$ 0.05, and amplitude $\geq$ 0.1) and more breaks ($\geq$1) were observed for water bodies and herbaceous wetlands. For Marais Vernier, the southern part (i.e., grassland and woodland) clearly differed from the northern part (i.e., cropland), which had larger RMSE (mean $\geq$ 7.80, SD $\geq$ 1.30, and amplitude $\geq$ 4.20) and more breaks ($\geq$2). For Ouled Saïd, bare soil and vegetated areas differed greatly, with the latter having a larger mean RMSE ($\geq$0.70) and amplitude ($\geq$0.10). Interestingly, the largest SD of RMSE and the highest number of breaks ($\geq$2) were observed in the center of the site along a northeast/southwest line, which corresponded to a depression (Figure 1). Site-specific stretching of these images also revealed linear patterns in the northwestern part that may have been due to the Landsat 7 SLC-off images. In comparison, Taiamã had many patches with large RMSE (mean $\geq$ 5.00, SD $\geq$ 0.50, and amplitude $\geq$ 5.00) and many breaks ($\geq$3). Similarly, for Pirttimysvuoma, these patches covered water bodies and herbaceous wetlands.

The ANOVA confirmed that LULC class had a large influence on NDVI-I accuracy for the four sites (η^2: 0.37–0.56), whereas the number of Landsat observations had a small influence on this value for Marais Vernier (η^2: 0.01) but a moderate influence on those for the other three sites (η^2: 0.09–0.12) (Table 2). The interaction between the two factors had a

small (η^2: 0.02–0.05) but significant influence on NDVI-I accuracy for Marais Vernier, Ouled Saïd, and Taiamã.

Table 2. Results of two-factor permutational analysis of variance to quantify the variance (expressed as mean partial eta-squared based on 500 iterations) in the accuracy (root-mean-square error) of the annual normalized difference vegetation index integral (NDVI-I) in 2021 for each Ramsar site explained by land use and land cover class (LULC), number of Landsat observations (NLO), and their interaction. *** $p < 0.001$, "ns" $p \geq 0.05$.

Ramsar Site	Factors		
	LULC	NLO	LULC × NLO
Pirttimysvuoma	0.37 ± 0.05 ***	0.10 ± 0.03 ***	ns
Marais Vernier	0.56 ± 0.03 ***	0.01 ± 0.01 ***	0.02 ± 0.01 ***
Ouled Saïd	0.40 ± 0.03 ***	0.09 ± 0.02 ***	0.05 ± 0.02 ***
Taiamã Ecological Station	0.37 ± 0.03 ***	0.12 ± 0.02 ***	0.05 ± 0.02 ***

Analysis of the interaction plots provided details about variations in NDVI-I accuracy as a function of LULC class and the number of Landsat observations (Figure 7). As expected, the mean RMSE was largest (≥3.40) for water bodies and cropland and smallest (<3.00) for tree cover, bare/sparse vegetation, and built-up areas. Interestingly, the RMSE values by LULC class were similar among the sites; for example, the mean RMSE for permanent water bodies ranged from 4.03 to 4.86 for Pirttimysvuoma and from 4.25 to 4.53 for Marais Vernier. The larger number of Landsat observations resulted in a smaller RMSE for permanent water bodies (Pirttimysvuoma and Taiamã), cropland (Marais Vernier), herbaceous wetland (Taiamã), and tree cover (Ouled Saïd and Taiamã).

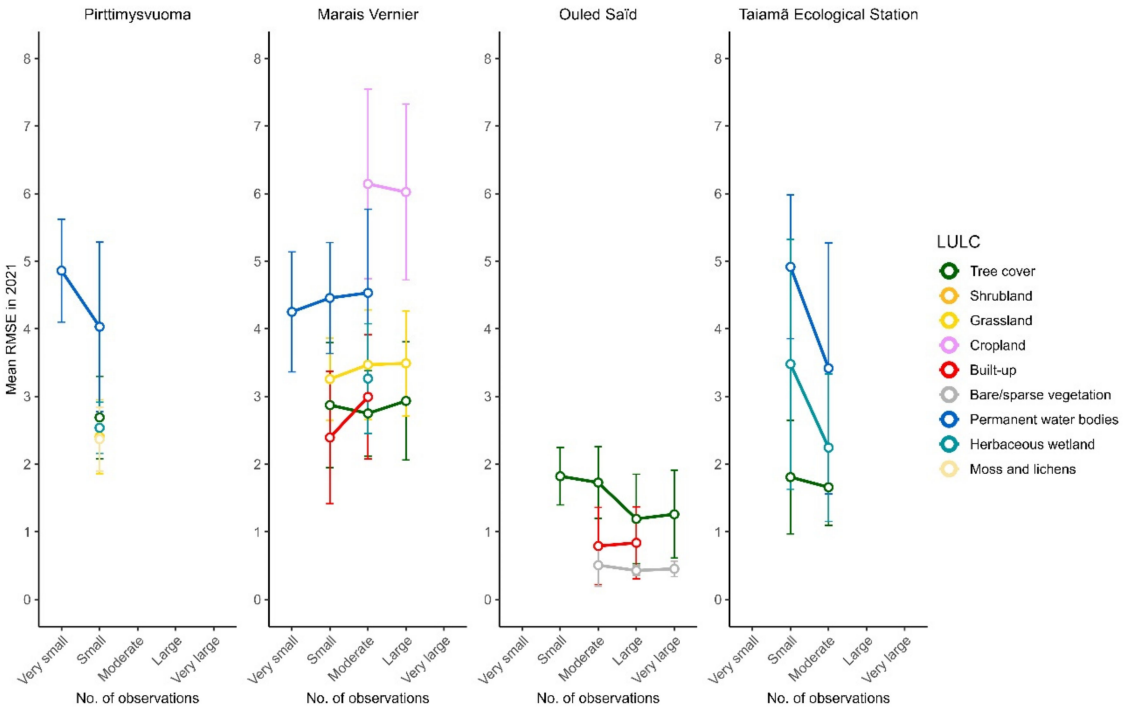

Figure 7. Influence of the number of Landsat observations (very small: 0–6; small: 7–19; moderate: 20–35; large: 36–63; very large: 64–113), land use and land cover (LULC) class, and their interaction on the accuracy of the continuous change detection and classification algorithm (median and standard deviation of the root-mean-square error (RMSE) for each wetland site). Lines that are nearly parallel indicate weak interactions.

3.2. Spatiotemporal Dynamics of NDVI-I

At the site scale, the temporal trends indicated that mean NDVI-I was highest for Taiamã (23.94–28.19) and Marais Vernier (19.45–22.26) and lowest for Pirttimysvuoma (16.76–20.18) and especially Ouled Saïd (2.85–3.16) (Figure 8). The mean annual NDVI-I increased over time, except for Ouled Saïd, whose trend was stable. In addition, spatial variability was higher for Marais Vernier (SD: 6.65–7.69) and Taiamã (SD: 4.74–6.11) than for Pirttimysvuoma (SD: 2.69–2.80) and Ouled Saïd (SD: 0.77–0.96).

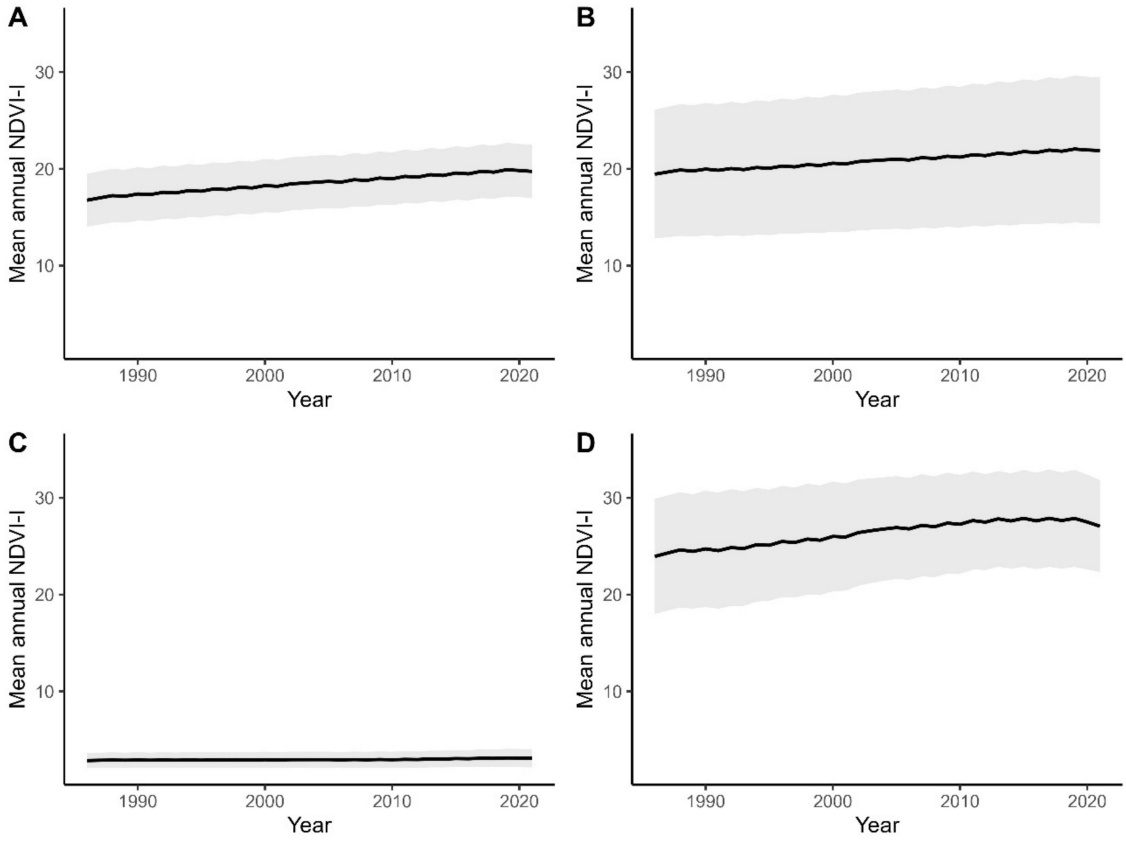

Figure 8. Annual variation in spatial mean annual normalized difference vegetation index integral (NDVI-I) (black line) and standard deviation of the annual variation in spatial mean NDVI-I (grey area) for each site for 1986–2021. (**A**) Pirttimysvuoma; (**B**) Marais Vernier; (**C**) Ouled Saïd; (**D**) Taiamã Ecological Station.

This high spatial variability in NDVI-I was highlighted at the pixel scale for each site (Figure 9). For Pirttimysvuoma, mean NDVI-I was highest for grassland (>21.40) and lowest ($\leq$1.50) for permanent water bodies. The variability in NDVI-I differed greatly among pixels, as illustrated by the fine-grained pattern of SD and amplitude images. NDVI-I tended to increase over time over nearly the entire site (minimum in ~1986, maximum in ~2021).

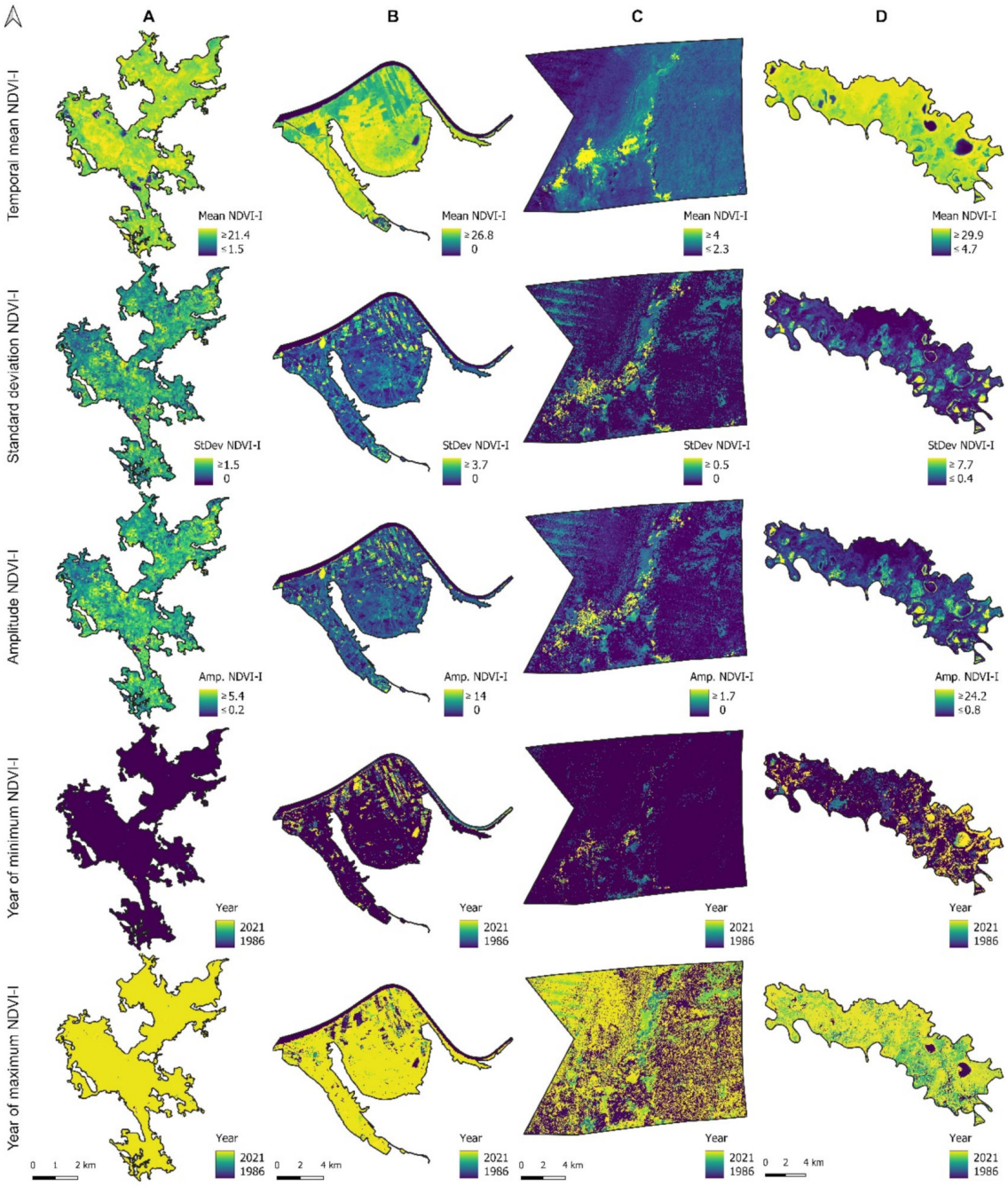

Figure 9. Temporal mean, standard deviation (StDev), amplitude (Amp.) of NDVI-I, and years of minimum and maximum NDVI-I for the four study sites for 1986–2021: (**A**) Pirttimysvuoma; (**B**) Marais Vernier; (**C**) Ouled Saïd; (**D**) Taiamã Ecological Station. Image stretching was applied to each site to highlight its spatial pattern.

For Marais Vernier, the mean NDVI-I was highest for grassland and tree cover (>26.80), lower for cropland (16.00–19.00), and lowest for water bodies ($\leq$3.00). The NDVI-I clearly varied the most over time for cropland (SD $\geq$ 2.50, amplitude $\geq$ 10.00). Unlike the rest of the site, cropland often had a decreasing trend in NDVI-I, with the minimum and maximum values observed in ~2021 and ~1986, respectively.

For Ouled Saïd, the mean NDVI-I was highest for vegetated areas ($\geq$4.00), intermediate in the central depression (3.00–3.50), and lowest throughout the rest of the site ($\leq$2.50). The NDVI-I generally varied little, although it varied more (SD $\geq$ 1.00, amplitude $\geq$ 3.00) for vegetated areas. Overall, NDVI-I increased over time, but the year with maximum

NDVI-I varied greatly among pixels. Interestingly, linear patterns were observed in the northwestern part, likely due to the Landsat 7 SLC-off images.

For Taiamã, the NDVI-I was highest for tree cover (≥29.00), lower for herbaceous wetland (22.00–27.00), and lowest for permanent water bodies (≤10.00). NDVI-I values varied more (SD ≥ 3.80, amplitude ≥ 8.00) for these flooded LULC classes. Overall, NDVI-I values increased over time (minimum ~1986, maximum ~2021), but they decreased for flooded classes (herbaceous wetlands and permanent water bodies).

3.3. Relationship between NDVI-I Temporal Trends and Climate

Correlations between the climate variables and the NDVI-I were significant (Table 3). For temperature variables, the mean annual T_{max} (r: 0.53–0.62) and, to a lesser extent, T_{mean} (r: 0.47–0.59) were strongly positively correlated with the annual NDVI-I for all sites, whereas the mean annual T_{min} was positively correlated only for Pirttimysvuoma and Marais Vernier (r = 0.39 and 0.57, respectively). P_{mm} was negatively correlated only with the annual mean NDVI-I for Taiamã (r = −0.38).

Table 3. Pearson correlations between annual mean NDVI-I and climate variables per study site. T_{min}: mean annual minimum temperature; T_{max}: mean annual maximum temperature; T_{mean}: mean annual mean temperature; P_{mm}: cumulative annual precipitation. * $p < 0.05$, ** $p < 0.01$, "ns" $p \geq 0.05$.

Climate Variable	Pirttimysvuoma	Marais Vernier	Oasis de Ouled Saïd	Taiamã Ecological Station
T_{min}	0.39 *	ns	0.57 **	ns
T_{max}	0.53 **	0.62 **	0.57 **	0.60 **
T_{mean}	0.47 **	0.49 **	0.59 **	0.51 **
P_{mm}	ns	ns	ns	−0.38 *

4. Discussion

The sensitivity of the CCDC algorithm can be influenced by the parameter values defined in the GEE API [21]. Consequently, we performed an exploratory calibration step before the analyses, as recommended by Pasquarella et al. [19]. Increasing the number of consecutive observations needed to identify a break (minObservations) from five (default value) to eight greatly decreased the number of breaks detected. Conversely, increasing the chi-square probability threshold at which changes were detected from 0.90 (default value) to 0.99 decreased the identification of false breaks. However, increasing the penalty parameter for LASSO regression lambda from 0.005 (default value) to 0.10 decreased the amplitude of the temporal profiles significantly. We decreased the maxIteration parameter from 25,000 to 10,000, as doing so slightly decreased calculation times without increasing the RMSE. This exploratory step demonstrated that the default parameters in the submit_CCDC script were generally appropriate. We could have performed site-specific hyper-calibration to increase the accuracy of the synthetic images, even though the CCDC algorithm is not highly sensitive to small parameter changes [19], but we used the same parameter values for all sites to emphasize the algorithm's generality. However, no break was identified for much of the Pirttimysvuoma and Marais Vernier sites, which seems unusual given the length of the study period and the dynamic characteristics of wetlands, which highlights the CCDC's limited ability to detect subtle changes, such as vegetation regrowth [19]. CCDC customizations such as DECODE (Detection and Characterization of Coastal Tidal Wetlands Change) have been developed recently to detect this type of change [52], but they have not yet been integrated into a cloud-based solution.

One major advantage of the CCDC algorithm over other approaches was its ability to use all Landsat archive images, including those with high cloud cover and/or SLC-off, to better capture wetland dynamics. For example, it was able to use 929 images for Taiamã instead of only the 91 images without clouds and was not influenced by the failure of the Landsat 7 SLC sensor. However, one disadvantage was that cloudy and noisy areas were over-masked at the expense of flooded areas, as indicated by the few Landsat

observations retained over water (Figure 1D). The over-detection of cloud shadows over water bodies was observed for CFmask [37], and although it was partially corrected in Fmask version 4.0 [53], it has not yet been integrated into the CCDC API of GEE. In addition, the Tmask used in CCDC sometimes confuses ephemeral floods with temporal artifacts. Because the developers of Tmask acknowledged this limitation [36], we initially considered disabling Tmask to better monitor flood dynamics, but preliminary tests indicated that it removed noise effectively from the time series.

Overall, using CCDC to simulate decadal synthetic NDVI images (from 1984 to 2021) enabled an accurate estimation of ANPP in wetlands. The results support previous studies that used CCDC to generate synthetic images for continuous monitoring of wetland ecosystem functioning over the long term [25]. However, Fu et al. [25] did not explore the sensitivity of the CCDC algorithm. The present study demonstrated that the accuracy (mean RMSE) of NDVI synthetic images ranged from 0.01 (0.46/36 dates) for the arid wetland to 0.11 (3.94/36 dates) for the tropical wetland. These results are similar to those of Liao et al. [24] for wooded vegetation in Australia (mean RMSE of 0.13 in the NIR band). The present study provided a deeper analysis, highlighting that the RMSE generally remained constant over time (1984–2021) but not over space. The high variations among and within sites were due to the LULC classes and the number of Landsat observations available.

Studies have recently highlighted the sensitivity of the CCDC algorithm to the number of observations available, but that number should be described more precisely than as "a sufficient number" [19]. The present study highlights that the increase in the number of Landsat images available (Figure 2), due to the launch of Landsat 7 in 1999 and Landsat-8 in 2013, has not increased the accuracy of the CCDC algorithm, except for Taiamã (Figure 5). For this site, which is covered by only one Landsat tile and thus had the fewest images, the mean and SD of the RMSE decreased significantly in the early 2000s. This period corresponds to the increase in the mean number of annual observations (from 12 for 1984–1999 to 33 for 2000–2021) due to the launch of Landsat 7. This result was not observed for Pirttimysvuoma, even though it also had few Landsat observations available. This may have been due to the contrasting dynamics of these sites: Pirttimysvuoma is covered mainly by extensive grasslands [54], whose relatively stable dynamics can be captured accurately with a few Landsat observations (6–19/years), unlike those of the herbaceous wetlands that are periodically flooded by the Paraguay River [55] and cover much of the Taiamã site (Figure 7). Thus, increasing the number of Landsat observations is the best way to increase the accuracy of CCDC for LULC classes with irregular or hazard-related dynamics, such as herbaceous wetlands, water bodies, and cropland.

The ANOVA indicated that the LULC class explained a large percentage of the variation in CCDC accuracy, likely due, as before, to the irregular and/or hazard-related dynamics of each LULC class caused by hydrodynamics and/or agricultural practices. CCDC was most accurate for the tree cover and grassland LULC classes, as they have relatively stable and linear dynamics. Interestingly, the RMSE for grasslands was larger for Marais Vernier, where grasslands were alternately grazed and mowed, which resulted in highly irregular seasonal cycles, than for Pirttimysvuoma, where grasslands were only grazed extensively. Conversely, the CCDC algorithm was less accurate for water bodies, herbaceous wetlands, and cropland, perhaps due to the algorithm itself, which assumes linear variations and constant amplitudes within a given time segment, which is not the case for crop rotations or floods. As reported by Liao et al. [24], this results in the over-detection of breaks and thus larger RMSE values (Figure 6). Approaches based on generalized additive models can also improve the continuous monitoring of frequently flooded areas [56], but these models are sensitive to outliers and discontinuous observations.

The present study identified a long-term increase in the NDVI-I at all four wetland sites, in coherence with the global "greening" phenomenon widely documented in the literature [57] and related to climate change, particularly in boreal regions [58]. Unsurprisingly, the Pirttimysvuoma boreal wetland showed the largest increase in the NDVI-I.

The greening phenomenon also occurred at Marais Vernier, accentuated by fertilizer inputs for agriculture [57]. At Taiamã, the greening phenomenon has been observed in the Pantanal [59], but NDVI-I values decreased in 2020 and 2021 (Figure 8), potentially due to drought and wildfires in 2020 [60]. Conversely, a relatively stable trend was observed for the arid Ouled Saïd site, which agrees with the observations of Wen et al. [56] for semi-arid marshes in Australia. However, recent studies of wetlands have highlighted that the greening phenomenon varies locally, with larger temporal amplitudes in water levels in flooded areas [25,56]. This was particularly evident for Taiamã, in which large amplitudes and negative trends in NDVI-I were observed in areas that flooded frequently (Figure 9) [61]. It also explains the negative correlation between rainfall and NDVI-I at Taiamã. Furthermore, the relationship between the NDVI and primary productivity can be biased in wetlands due to the decrease in spectral reflectance caused by water absorption [26]. Although the present study addressed this bias for flooded areas by reclassifying negative NDVI values to zero, it may remain for semi-submerged vegetated areas.

This study shows that the implemented method for the long-term monitoring of wetland ecosystem functioning is robust under contrasting bioclimatic conditions. The method is based on the cloud computing use of a large volume of open access satellite data and algorithms, making it an easily accessible tool to improve the long-term monitoring and management of wetlands considering the dimension of their ecosystem functioning [7–9]. For example, this tool could improve the implementation of target 5 "maintenance of ecological character" of the Ramsar Strategic Plan 2016–2024 [3], Aichi target 1 "conserve biodiversity" of the Convention on Biological Diversity [4], or target 6.6 "protect and restore water-related ecosystems" of the UN Sustainable Development Goals [5].

Author Contributions: Conceptualization, S.R.; formal analysis, Q.D.; methodology, S.R. and L.H.-M.; supervision, L.H.-M.; writing—original draft preparation, Q.D., S.R. and L.H.-M.; writing—review and editing, D.A. and S.C. All authors have read and agreed to the published version of the manuscript.

Funding: Q.D. received a Ph.D. grant (2021–2024) from the French Ministry of Higher Education, Research, and Innovation.

Institutional Review Board Statement: Not applicable.

Informed Consent Statement: Not applicable.

Data Availability Statement: Dataset available upon request from the authors.

Acknowledgments: The authors acknowledge the U.S. Geological Survey for making the Landsat data freely available.

Conflicts of Interest: The authors declare no conflicts of interest.

Appendix A

Table A1. Summary of the number of available images per Landsat sensor and per tile for each study site for the 1984–2021 study period. ES: Ecological Station.

Sensor	Pirttimysvuoma			Marais Vernier				Ouled Saïd			Taiamã ES
	194/12	195/12	196/12	197/12	200/26	201/25	201/26	196/40	197/39	197/40	222/72
L4–5 TM	106	61	96	110	222	342	237	426	352	365	344
L7 ETM+	143	139	137	128	237	332	245	318	331	330	419
L8–9 OLI/TIRS	73	87	79	104	129	197	149	198	197	198	166

References

1. Xu, X.; Chen, M.; Yang, G.; Jiang, B.; Zhang, J. Wetland Ecosystem Services Research: A Critical Review. *Glob. Ecol. Conserv.* **2020**, *22*, e01027. [CrossRef]
2. Fluet-Chouinard, E.; Stocker, B.D.; Zhang, Z.; Malhotra, A.; Melton, J.R.; Poulter, B.; Kaplan, J.O.; Goldewijk, K.K.; Siebert, S.; Minayeva, T.; et al. Extensive Global Wetland Loss over the Past Three Centuries. *Nature* **2023**, *614*, 281–286. [CrossRef] [PubMed]

3. Ramsar Convention on Wetlands Scaling Up Wetland Conservation, Wise Use and Restoration to Achieve the Sustainable Developmenct Goals. 2018. Available online: https://ramsar.org/sites/default/files/documents/library/cop12_res02_strategic_plan_e_0.pdf (accessed on 17 July 2024).
4. CBD Secretariat. *The Strategic Plan for Biodiversity 2011–2020 and the Aichi Biodiversity Targets*; Secretariat of the Convention on Biological Diversity: Nagoya, Japan, 2010.
5. United Nations. Transforming Our World: The 2030 Agenda for Sustainable Development. In *Outcome Document for the UN Summit to Adopt the Post-2015 Development Agenda*; United Nations: New York, NY, USA, 2015.
6. Viñuales, J.E. The Paris Agreement on Climate Change. *Ger. YB Int'l L* **2016**, *59*, 11.
7. Geijzendorffer, I.R.; Beltrame, C.; Chazee, L.; Gaget, E.; Galewski, T.; Guelmami, A.; Perennou, C.; Popoff, N.; Guerra, C.A.; Leberger, R.; et al. A More Effective Ramsar Convention for the Conservation of Mediterranean Wetlands. *Front. Ecol. Evol.* **2019**, *7*, 21. [CrossRef]
8. Lock, M.C.; Skidmore, A.K.; van Duren, I.; Mücher, C.A. Evidence-Based Alignment of Conservation Policies with Remote Sensing-Enabled Essential Biodiversity Variables. *Ecol. Indic.* **2021**, *132*, 108272. [CrossRef]
9. Kingsford, R.T.; Bino, G.; Finlayson, C.M.; Falster, D.; Fitzsimons, J.A.; Gawlik, D.E.; Murray, N.J.; Grillas, P.; Gardner, R.C.; Regan, T.J.; et al. Ramsar Wetlands of International Importance–Improving Conservation Outcomes. *Front. Environ. Sci.* **2021**, *9*, 643367. [CrossRef]
10. Jones, K.; Lanthier, Y.; van der Voet, P.; van Valkengoed, E.; Taylor, D.; Fernandez-Prieto, D. Monitoring and Assessment of Wetlands Using Earth Observation: The GlobWetland Project. *J. Environ. Manag.* **2009**, *90*, 2154–2169. [CrossRef] [PubMed]
11. Weise, K.; Höfer, R.; Franke, J.; Guelmami, A.; Simonson, W.; Muro, J.; O'Connor, B.; Strauch, A.; Flink, S.; Eberle, J.; et al. Wetland Extent Tools for SDG 6.6.1 Reporting from the Satellite-Based Wetland Observation Service (SWOS). *Remote Sens. Environ.* **2020**, *247*, 111892. [CrossRef]
12. MacKay, H.; Finlayson, C.M.; Fernandez-Prieto, D.; Davidson, N.; Pritchard, D.; Rebelo, L.-M. The Role of Earth Observation (EO) Technologies in Supporting Implementation of the Ramsar Convention on Wetlands. *J. Environ. Manag.* **2009**, *90*, 2234–2242. [CrossRef] [PubMed]
13. Rebelo, L.-M.; Finlayson, C.M.; Strauch, A.; Rosenqvist, A.; Perennou, C.; Tottrup, C.; Hilarides, L.; Paganini, M.; Wielaard, N.; Siegert, F. *The Use of Earth Observation for Wetland Inventory, Assessment and Monitoring*; Ramsar Technical Report 10; Ramsar Convention Secretariat: Gland, Switzerland, 2018; p. 31. Available online: https://cgspace.cgiar.org/server/api/core/bitstreams/bd68d105-ad61-4d5f-8d5e-f06229a6d4fe/content (accessed on 17 July 2024).
14. Wulder, M.A.; Roy, D.P.; Radeloff, V.C.; Loveland, T.R.; Anderson, M.C.; Johnson, D.M.; Healey, S.; Zhu, Z.; Scambos, T.A.; Pahlevan, N. Fifty Years of Landsat Science and Impacts. *Remote Sens. Environ.* **2022**, *280*, 113195. [CrossRef]
15. Woodcock, C.E.; Allen, R.; Anderson, M.; Belward, A.; Bindschadler, R.; Cohen, W.; Gao, F.; Goward, S.N.; Helder, D.; Helmer, E.; et al. Free Access to Landsat Imagery. *Science* **2008**, *320*, 1011. [CrossRef] [PubMed]
16. Mutanga, O.; Kumar, L. Google Earth Engine Applications. *Remote Sens.* **2019**, *11*, 591.
17. Demarquet, Q.; Rapinel, S.; Dufour, S.; Hubert-Moy, L. Long-Term Wetland Monitoring Using the Landsat Archive: A Review. *Remote Sens.* **2023**, *15*, 820. [CrossRef]
18. Li, S.; Xu, L.; Jing, Y.; Yin, H.; Li, X.; Guan, X. High-Quality Vegetation Index Product Generation: A Review of NDVI Time Series Reconstruction Techniques. *Int. J. Appl. Earth Obs. Geoinf.* **2021**, *105*, 102640. [CrossRef]
19. Pasquarella, V.J.; Arévalo, P.; Bratley, K.H.; Bullock, E.L.; Gorelick, N.; Yang, Z.; Kennedy, R.E. Demystifying LandTrendr and CCDC Temporal Segmentation. *Int. J. Appl. Earth Obs. Geoinf.* **2022**, *110*, 102806. [CrossRef]
20. Awty-Carroll, K.; Bunting, P.; Hardy, A.; Bell, G. An Evaluation and Comparison of Four Dense Time Series Change Detection Methods Using Simulated Data. *Remote Sens.* **2019**, *11*, 2779. [CrossRef]
21. Arévalo, P.; Bullock, E.L.; Woodcock, C.E.; Olofsson, P. A Suite of Tools for Continuous Land Change Monitoring in Google Earth Engine. *Front. Clim.* **2020**, *2*, 576740. [CrossRef]
22. Cabello, J.; Fernández, N.; Alcaraz-Segura, D.; Oyonarte, C.; Pineiro, G.; Altesor, A.; Delibes, M.; Paruelo, J.M. The Ecosystem Functioning Dimension in Conservation: Insights from Remote Sensing. *Biodivers. Conserv.* **2012**, *21*, 3287–3305. [CrossRef]
23. Arévalo, P.; Baccini, A.; Woodcock, C.E.; Olofsson, P.; Walker, W.S. Continuous Mapping of Aboveground Biomass Using Landsat Time Series. *Remote Sens. Environ.* **2023**, *288*, 113483. [CrossRef]
24. Liao, Z.; Liu, X.; van Dijk, A.; Yue, C.; He, B. Continuous Woody Vegetation Biomass Estimation Based on Temporal Modeling of Landsat Data. *Int. J. Appl. Earth Obs. Geoinf.* **2022**, *110*, 102811. [CrossRef]
25. Fu, B.; Lan, F.; Yao, H.; Qin, J.; He, H.; Liu, L.; Huang, L.; Fan, D.; Gao, E. Spatio-Temporal Monitoring of Marsh Vegetation Phenology and Its Response to Hydro-Meteorological Factors Using CCDC Algorithm with Optical and SAR Images: In Case of Honghe National Nature Reserve, China. *Sci. Total Environ.* **2022**, *843*, 156990. [CrossRef] [PubMed]
26. Bansal, S.; Creed, I.F.; Tangen, B.A.; Bridgham, S.D.; Desai, A.R.; Krauss, K.W.; Neubauer, S.C.; Noe, G.B.; Rosenberry, D.O.; Trettin, C. Practical Guide to Measuring Wetland Carbon Pools and Fluxes. *Wetlands* **2023**, *43*, 105. [PubMed]
27. Radeloff, V.C.; Dubinin, M.; Coops, N.C.; Allen, A.M.; Brooks, T.M.; Clayton, M.K.; Costa, G.C.; Graham, C.H.; Helmers, D.P.; Ives, A.R. The Dynamic Habitat Indices (Dhis) from Modis and Global Biodiversity. *Remote Sens. Environ.* **2019**, *222*, 204–214. [CrossRef]

28. Dąbrowska-Zielińska, K.; Misiura, K.; Malińska, A.; Gurdak, R.; Grzybowski, P.; Bartold, M.; Kluczek, M. Spatiotemporal Estimation of Gross Primary Production for Terrestrial Wetlands Using Satellite and Field Data. *Remote Sens. Appl. Soc. Environ.* **2022**, *27*, 100786. [CrossRef]
29. Rapinel, S.; Fabre, E.; Dufour, S.; Arvor, D.; Mony, C.; Hubert-Moy, L. Mapping Potential, Existing and Efficient Wetlands Using Free Remote Sensing Data. *J. Environ. Manag.* **2019**, *247*, 829–839. [CrossRef] [PubMed]
30. Pettorelli, N.; Vik, J.O.; Mysterud, A.; Gaillard, J.-M.; Tucker, C.J.; Stenseth, N.C. Using the Satellite-Derived NDVI to Assess Ecological Responses to Environmental Change. *Trends Ecol. Evol.* **2005**, *20*, 503–510. [CrossRef] [PubMed]
31. Fernandez-Carrillo, A.; Sanchez-Rodriguez, E.; Rodriguez-Galiano, V.F. Characterising Marshland Temporal Dynamics Using Remote Sensing: The Case of Bolboschoenetum Maritimi in Doñana National Park. *Appl. Geogr.* **2019**, *112*, 102094. [CrossRef]
32. Zhang, L.; Wu, Z.; Chen, J.; Liu, D.; Chen, P. Spatiotemporal Patterns and Drivers of Net Primary Production in the Terrestrial Ecosystem of the Dajiuhu Basin, China, between 1990 and 2018. *Ecol. Inform.* **2022**, *72*, 101839. [CrossRef]
33. Landsberg, H.; Pinna, M. *L'atmosfera e il Clima*; UTET: Turin, Italy, 1978.
34. Lubke, M.; Rengarajan, R.; Choate, M. Preliminary Assessment of the Geometric Improvements to the Landsat Collection-2 Archive. In *Earth Observing Systems XXVI*; SPIE: Bellingham, MA, USA, 2021; Volume 11829, pp. 125–137. [CrossRef]
35. Gorelick, N.; Hancher, M.; Dixon, M.; Ilyushchenko, S.; Thau, D.; Moore, R. Google Earth Engine: Planetary-Scale Geospatial Analysis for Everyone. *Remote Sens. Environ.* **2017**, *202*, 18–27. [CrossRef]
36. Zhu, Z.; Woodcock, C.E. Continuous Change Detection and Classification of Land Cover Using All Available Landsat Data. *Remote Sens. Environ.* **2014**, *144*, 152–171. [CrossRef]
37. Foga, S.; Scaramuzza, P.L.; Guo, S.; Zhu, Z.; Dilley, R.D., Jr.; Beckmann, T.; Schmidt, G.L.; Dwyer, J.L.; Hughes, M.J.; Laue, B. Cloud Detection Algorithm Comparison and Validation for Operational Landsat Data Products. *Remote Sens. Environ.* **2017**, *194*, 379–390. [CrossRef]
38. Zhu, Z.; Woodcock, C.E. Object-Based Cloud and Cloud Shadow Detection in Landsat Imagery. *Remote Sens. Environ.* **2012**, *118*, 83–94. [CrossRef]
39. Zanaga, D.; Van De Kerchove, R.; Daems, D.; De Keersmaecker, W.; Brockmann, C.; Kirches, G.; Wevers, J.; Cartus, O.; Santoro, M.; Fritz, S.; et al. ESA WorldCover 10 m 2021 V200 2022, Dataset, Zenodo. Available online: https://pure.iiasa.ac.at/id/eprint/18478/ (accessed on 17 July 2024).
40. Menne, M.J.; Durre, I.; Vose, R.S.; Gleason, B.E.; Houston, T.G. An Overview of the Global Historical Climatology Network-Daily Database. *J. Atmos. Ocean. Technol.* **2012**, *29*, 897–910. [CrossRef]
41. NOAA Gridded Climate: NOAA Physical Sciences Laboratory. Available online: https://psl.noaa.gov/data/gridded/ (accessed on 30 August 2023).
42. Zhu, Z.; Woodcock, C.E. Automated Cloud, Cloud Shadow, and Snow Detection in Multitemporal Landsat Data: An Algorithm Designed Specifically for Monitoring Land Cover Change. *Remote Sens. Environ.* **2014**, *152*, 217–234. [CrossRef]
43. Tibshirani, R. Regression Shrinkage and Selection Via the Lasso. *J. R. Stat. Soc. Ser. B* **1996**, *58*, 267–288. [CrossRef]
44. Zhu, Z.; Woodcock, C.E.; Holden, C.; Yang, Z. Generating Synthetic Landsat Images Based on All Available Landsat Data: Predicting Landsat Surface Reflectance at Any given Time. *Remote Sens. Environ.* **2015**, *162*, 67–83. [CrossRef]
45. Alcaraz, D.; Paruelo, J.; Cabello, J. Identification of Current Ecosystem Functional Types in the Iberian Peninsula. *Glob. Ecol. Biogeogr.* **2006**, *15*, 200–212. [CrossRef]
46. Anderson, M.J. Permutational Multivariate Analysis of Variance (PERMANOVA). In *Wiley StatsRef: Statistics Reference Online*; John Wiley & Sons: Hoboken, NJ, USA, 2014; pp. 1–15.
47. Richardson, J.T.E. Eta Squared and Partial Eta Squared as Measures of Effect Size in Educational Research. *Educ. Res. Rev.* **2011**, *6*, 135–147. [CrossRef]
48. R Core Team. R: A Language and Environment for Statistical Computing, R Foundation for Statistical Computing, Vienna, Austria. Available online: https://www.r-project.org/ (accessed on 17 July 2024).
49. Hijmans, R. Terra: Spatial Data Anaysis. Available online: https://rspatial.github.io/terra/ (accessed on 17 July 2024).
50. Lê, S.; Josse, J.; Husson, F. FactoMineR: A Package for Multivariate Analysis. *J. Stat. Softw.* **2008**, *25*, 1–18. [CrossRef]
51. Wheeler, B.; Torchiano, M.; Torchiano, M.M. Package 'lmPerm'. Available online: https://cran.r-project.org/web/packages/lmPerm/lmPerm.pdf (accessed on 17 July 2024).
52. Yang, X.; Zhu, Z.; Qiu, S.; Kroeger, K.D.; Zhu, Z.; Covington, S. Detection and Characterization of Coastal Tidal Wetland Change in the Northeastern US Using Landsat Time Series. *Remote Sens. Environ.* **2022**, *276*, 113047. [CrossRef]
53. Qiu, S.; Zhu, Z.; He, B. Fmask 4.0: Improved Cloud and Cloud Shadow Detection in Landsats 4–8 and Sentinel-2 Imagery. *Remote Sens. Environ.* **2019**, *231*, 111205. [CrossRef]
54. Pirttimysvuoma | Ramsar Sites Information Service. Available online: https://rsis.ramsar.org/ris/2177?language=en (accessed on 9 March 2023).
55. Frota, A.V.B.d.; Ikeda-Castrillon, S.K.; Kantek, D.L.Z.; da Silva, C.J. Macro-habitats of the Taiamã Ecological Station, in the context of the Pantanal wetland, Brazil. *Bol. Mus. Para. Emílio Goeldi Ciências Nat.* **2017**, *12*, 239–254.
56. Wen, L.; Mason, T.J.; Ryan, S.; Ling, J.E.; Saintilan, N.; Rodriguez, J. Monitoring Long-Term Vegetation Condition Dynamics in Persistent Semi-Arid Wetland Communities Using Time Series of Landsat Data. *Sci. Total Environ.* **2023**, *905*, 167212. [CrossRef] [PubMed]

57. Piao, S.; Wang, X.; Park, T.; Chen, C.; Lian, X.; He, Y.; Bjerke, J.W.; Chen, A.; Ciais, P.; Tømmervik, H.; et al. Characteristics, Drivers and Feedbacks of Global Greening. *Nat. Rev. Earth Environ.* **2020**, *1*, 14–27. [CrossRef]
58. Ju, J.; Masek, J.G. The Vegetation Greenness Trend in Canada and US Alaska from 1984–2012 Landsat Data. *Remote Sens. Environ.* **2016**, *176*, 1–16. [CrossRef]
59. De Souza Miranda, C.; Cândido, A.K.A.A.; Mioto, C.L.; da Silva, N.M.; Paranhos Filho, A.C.; Pott, A. Geotechnology as Support for the Management of Conservation Units in Brazil's Pantanal. *Bol. Mus. Para. Emílio Goeldi-Ciências Nat.* **2017**, *12*, 255–264.
60. Correa, D.B.; Alcântara, E.; Libonati, R.; Massi, K.G.; Park, E. Increased Burned Area in the Pantanal over the Past Two Decades. *Sci. Total Environ.* **2022**, *835*, 155386. [CrossRef] [PubMed]
61. Ivory, S.J.; McGlue, M.M.; Spera, S.; Silva, A.; Bergier, I. Vegetation, Rainfall, and Pulsing Hydrology in the Pantanal, the World's Largest Tropical Wetland. *Environ. Res. Lett.* **2019**, *14*, 124017. [CrossRef]

Disclaimer/Publisher's Note: The statements, opinions and data contained in all publications are solely those of the individual author(s) and contributor(s) and not of MDPI and/or the editor(s). MDPI and/or the editor(s) disclaim responsibility for any injury to people or property resulting from any ideas, methods, instructions or products referred to in the content.